Nuclear Medicine and Biology 106–107 (2022) 10–20

Contents lists available at ScienceDirect

Nuclear Medicine and Biology

journal homepage: www.elsevier.com/locate/nucmedbio

# Dose estimation after a mixed field exposure: Radium-223 and intensity modulated radiotherapy

Isabella Bastiani [a,*], Stephen J. McMahon [b], Philip Turner [b,c], Kelly M. Redmond [c], Conor K. McGarry [b,c], Aidan Cole [b,c], Joe M. O'Sullivan [b,c], Kevin M. Prise [b], Liz Ainsbury [d], Rhona Anderson [a]

[a] Centre for Health Effects of Radiological and Chemical Agents, College of Health, Medicine and Life Sciences, Brunel University London, Kingston Lane, Uxbridge, London UB8 3PH, United Kingdom of Great Britain and Northern Ireland
[b] Patrick G. Johnston Centre for Cancer Research, Queen's University Belfast, Belfast BT9 7AE, United Kingdom of Great Britain and Northern Ireland
[c] Northern Ireland Cancer Centre, Belfast Health and Social Care Trust, Belfast, United Kingdom of Great Britain and Northern Ireland
[d] Centre for Radiation, Chemical & Environmental Hazards, Public Health England, Didcot OX11 0RQ, United Kingdom of Great Britain and Northern Ireland

ARTICLE INFO

*Article history:*
Received 17 February 2021
Received in revised form 4 November 2021
Accepted 9 December 2021
Available online xxxx

*Keywords:*
Radium-223
Biodosimetry
Chromosome exchanges
Targeted alpha-particle therapy
Prostate cancer

ABSTRACT

*Introduction:* Radium-223 dichloride ([$^{223}$Ra]$RaCl_2$), a radiopharmaceutical that delivers α-particles to regions of bone metastatic disease, has been proven to improve overall survival of men with metastatic castration resistant prostate cancer (mCRPC). mCRPC patients enrolled on the ADRRAD clinical trial are treated with a mixed field exposure comprising radium-223 ($^{223}$Ra) and intensity modulated radiotherapy (IMRT). While absorbed dose estimation is an important step in the characterisation of wider systemic radiation risks in nuclear medicine, uncertainties remain for novel radiopharmaceuticals such as $^{223}$Ra.

*Methods:* 24-Colour karyotyping was used to quantify the spectrum of chromosome aberrations in peripheral blood lymphocytes of ADRRAD patients at incremental times during their treatment. Dicentric equivalent frequencies were used in standard models for estimation of absorbed blood dose. To account for the mixed field nature of the treatment, existing models were used to determine the ratio of the component radiation types. Additionally, a new approach (M-$FISH_{LET}$), based on the ratio of cells containing damage consistent with high-LET exposure (complex chromosomal exchanges) and low-LET exposure (simple exchanges), was used as a pseudo ratio for $^{223}$Ra:IMRT dose.

*Results:* Total IMRT estimated doses delivered to the blood after completion of mixed radiotherapy (after 37 IMRT fractions and two [$^{223}$Ra]$RaCl_2$ injections) were in the range of 1.167 ± 0.092 and 2.148 ± 0.096 Gy (dose range across all models applied). By the last treatment cycle analysed in this study (four [$^{223}$Ra]$RaCl_2$ injections), the total absorbed $^{223}$Ra dose to the blood was estimated to be between 0.024 ± 0.027 and 0.665 ± 0.080 Gy, depending on the model used. Differences between the models were observed, with the observed dose variance coming from inter-model as opposed to inter-patient differences. The M-$FISH_{LET}$ model potentially overestimates the $^{223}$Ra absorbed blood dose by accounting for further PBL exposure in the vicinity of metastatic sites.

*Conclusions:* The models presented provide initial estimations of cumulative dose received during incremental IMRT fractions and [$^{223}$Ra]$RaCl_2$ injections, which will enable improved understanding of the doses received by individual patients. While the M-$FISH_{LET}$ method builds on a well-established technique for external exposures, further consideration is needed to evaluate this method and its use in assessing non-targeted exposure by $^{223}$Ra after its localization at bone metastatic sites.



## 1. Introduction

Metastatic castration resistant prostate cancer (mCRPC) is an incurable condition. Prostate cancer has a strong predisposition to forming bone metastases, with upwards of 90% of patients with advanced disease being affected, often with bone as the only site of metastasis [1]. As the general standard of care in the UK, patients with mCRPC are offered a number of life-prolonging therapies including chemotherapy,

* Corresponding author.
*E-mail addresses:* isabella.bastiani@brunel.ac.uk (I. Bastiani), stephen.mcmahon@qub.ac.uk (S.J. McMahon), philip.turner@cantab.net (P. Turner), kelly.redmond@qub.ac.uk (K.M. Redmond), conor.mcgarry@belfasttrust.hscni.net (C.K. McGarry), a.cole@qub.ac.uk (A. Cole), joe.osullivan@qub.ac.uk (J.M. O'Sullivan), k.prise@qub.ac.uk (K.M. Prise), liz.ainsbury@phe.gov.uk (L. Ainsbury), rhona.anderson@brunel.ac.uk (R. Anderson).

https://doi.org/10.1016/j.nucmedbio.2021.12.002

novel anti-hormonals and Radium-223 dichloride ([$^{223}$Ra]$RaCl_2$). Recent advances in molecular radiotherapy have generated a great deal of interest, particularly the use of [$^{223}$Ra]$RaCl_2$ after the landmark phase III trial ALSYMPCA [2–4] showed for the first time an overall survival advantage associated with [$^{223}$Ra]$RaCl_2$ treatment. Along with survival prolongation, this trial also demonstrated significant improvement in the quality of life by delaying the onset of symptomatic skeletal related events and alleviating pain. This led to FDA and EMA approvals and the widespread use of [$^{223}$Ra]$RaCl_2$ for symptomatic mCRPC [5,6]. $^{223}$Ra has a half-life of 11.43 days, decaying through creation of a succession of short-lived nuclides to stable $^{207}$Pb. During its decay chain, $^{223}$Ra emits four α and two β particles, with 94% of its decay energy released as high LET α-particles over a short track length of <100 μm [7,8]. When living tissue is exposed to $^{223}$Ra, this results in the localized induction of clustered DSB lesions which are difficult to repair, effectively leading to cell death [9–11].

For symptomatic mCRPC patients, $^{223}$Ra is administered intravenously as [$^{223}$Ra]$RaCl_2$ under the trade name of Xofigo [5]. Once administered, [$^{223}$Ra]$RaCl_2$ immediately solubilises in the blood resulting in free $^{223}$Ra, which as a calcium mimetic, is cleared from the blood within 24 h (h) [12] localising to areas of freshly mineralized bone. The uptake of $^{223}$Ra into high-turnover areas of bone is not dependent on a particular malignant signalling process. Thus, [$^{223}$Ra]$RaCl_2$ could be of benefit in a range of other malignancies which have a predisposition to forming bony metastases such as breast, lung, kidney and myeloma, including those with favourable long-term survival probability. Due to the short range of α-particles, this effective target cell kill also minimises direct α-particle exposure to non-target normal cells [7,13–16]. There is also evidence, however, that $^{223}$Ra can lead to high absorbed doses in sites adjacent to target bone metastases, including osteogenic cells and the red bone marrow [17–20]. It has also been reported that additional biological responses via bystander effects may also occur [21].

Currently, the number of studies which seek to understand the biological action of $^{223}$Ra *in vivo* in humans is limited [22], indeed, there remains a lack of scientific rationale to underpin current dosing strategies and there remains a great deal of uncertainty about the heterogeneous distribution of dose at the cellular and tissue levels and the role of direct and indirect effects such as bystander responses. Exposure of non-cancerous cells and tissues surrounding the tumours is of concern in all radiotherapeutic treatments, due to acute toxicity and the potential for delayed late effects, sometimes many years after treatment [23–30]. Quantifying the absorbed dose to non-target tissues is an important step in evaluating the potential short- and longer-term secondary radiation risks for patients [31]. This is of particular importance if [$^{223}$Ra]$RaCl_2$ is to be used earlier in the treatment schedule. A number of dose calculation models have been developed, for example, for calculation of the absorbed dose to blood from radiotherapy [32], however the actual or estimated consequences of these are still being quantified [33].

Cytogenetic analysis of chromosome aberrations in blood lymphocytes is widely used to estimate the dose of ionising radiation received by an individual following a real or suspected radiation overexposure, to help inform assessment of future health risks [34,35]. The dicentric assay is the most common method of biological dosimetry, not least due to the high radiation specificity and low interindividual variation between yields of dicentric chromosome aberrations [34]. In so called criticality situations of mixed field neutron and gamma exposures after nuclear reactor incidents, where individuals are irradiated by both high-LET and low-LET sources, a model for emergency exposure situations has been designed to estimate external doses for the individual exposure components [35]. Although originally designed for mixed neutron:gamma exposures, for medical uses of radiation, the ratios of delivered doses from internal and externally applied radiations can be readily derived from patient treatment plans. Meaning that this approach can be applied to calculate alpha and X-ray doses in cases of mixed exposures. Complex chromosome aberrations are useful biomarkers of LET [36], and their identification in exposed individuals could provide another approach for estimating the doses from mixed exposures and, thus, to further refine dose estimation methods in mixed exposure scenarios.

ADDRAD is an approved (NHS REC 15/NI/0074) phase I/II clinical trial which seeks to address the potential benefit of treating metastatic hormone sensitive prostate cancer patients with androgen deprivation therapy in addition to 6 cycles of [$^{223}$Ra]$RaCl_2$ and intensity modulated radiotherapy (IMRT) to the prostate and pelvic lymph nodes which has recently reported its first clinical data showing good response and minimal toxicity [37]. This patient group therefore presents a unique opportunity to address important radiobiological research questions pertaining to the doses and cellular and tissue level damage associated with internal $^{223}$Ra exposure combined with IMRT. In this study, we describe the use of 24-colour whole chromosome painting (multiplex fluorescence *in situ* hybridisation, M-FISH) applied to blood samples taken from the ADRRAD cohort of patients, to quantify the patterns of chromosome exchange complexity, with the aim of discriminating damaged cells from each component radiation type and estimating absorbed radiation dose. In addition, patient specific information is used to calculate absorbed doses to blood on the basis of three different established or adapted models, and the dose estimates are compared, with the overall aim to further understand the uncertainties involved in dose estimation in this mixed radiation exposure scenario.

## 2. Methods

### 2.1. Physically derived blood dose estimates

The absorbed blood dose per fraction ($D_b$) was estimated using data from 13 recruited mCRPC patients. [$^{223}$Ra]$RaCl_2$ was administered over 6 cycles (C1–C6), comprised of one intravenous injection every 4 weeks containing 55 kBq kg$^{-1}$ of $^{223}$Ra [38] (Fig. 1). As part of the treatment, IMRT is received during the first 7.5 weeks, coinciding with two [$^{223}$Ra]$RaCl_2$ cycles. The IMRT treatment plan for ADRRAD targets the prostate with a dose of 74 Gy, with 60 Gy delivered to lymph nodes. IMRT was delivered in daily fractions of 2 Gy to the prostate and 1.6 Gy to the lymph nodes, the latter as a concomitant boost. Individualised patient treatment schedules are outlined in supplementary Table 1. The absorbed dose to the blood was estimated for $^{223}$Ra based on its pharmacokinetic properties, and the IMRT dose by two

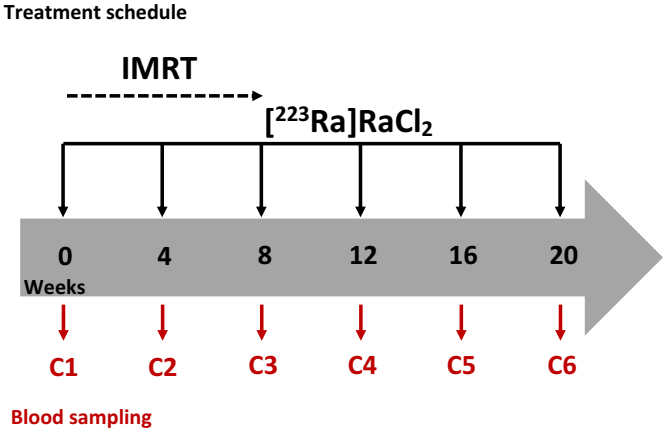


**Fig. 1.** Treatment timeline. IMRT daily fractions for 7.5 weeks. [$^{223}$Ra]$RaCl_2$ was administered every 4 weeks for a total of 6 injections. Blood samples were collected at each cycle, with a control sample collected at week 0 prior to treatment start (C1). Subsequent blood samples were taken every 4 weeks just prior to the next [$^{223}$Ra]$RaCl_2$ administration, up to C6. Hence blood samples from C2 and C3 are representative of mixed field exposure while C4–C6 are $^{223}$Ra only. For this study only samples up to C5 were analysed.

simple blood dose models originally derived by Moquet et al. [32] with modifications as described.

*2.1.1. Pharmacokinetic derived absorbed blood dose of $^{223}$Ra*

In the ADDRAD trial, [$^{223}$Ra]$RaCl_2$ was administered at an activity of 55 kBq kg$^{-1}$ of total body weight. Following this, the radionuclide will clear from the blood by 24 h. Previous studies identified the amount of $^{223}$Ra in the whole blood volume at varying time points within 24 h of administration [12,39–41]. The median percentage of circulating $^{223}$Ra was averaged at timepoints of 15 min, 4 h and 24 h between all studies reporting median values with upper and lower ranges [39–41]. This gave estimates for the percentage of radium in the blood of 22% after 15 min (9–28%), 3% (1.3–4.95%) after 4 h and 0.8% (0.37–1%) at 24 h. This information was used to estimate the physical absorbed dose to the blood by circulating $^{223}$Ra.

Firstly, the total activity of $^{223}$Ra present in the blood was estimated at each timepoint. This was determined by multiplying the initial injected activity of radium by the estimated percentage of $^{223}$Ra remaining in the blood and the decay constant of $^{223}$Ra, $7.02 \times 10^{-7}$ s$^{-1}$ [42]. The rate of energy deposition was then calculated using the energy release for each decay of $^{223}$Ra and its short-lived daughter products ($^{219}$Rn, $^{215}$Po and $^{211}$Bi) [43], with the total α-particle energy release estimated to be $4.30 \times 10^{-12}$ J. Finally, the dose rate to blood was calculated by dividing this rate of energy deposition by the mass of blood of the patient, which for this work was estimated using 75 ml of blood per kg body weight.

The absorbed dose rates were then plotted as a function of time following injection, and the area under the curve was calculated (GraphPad Prism 9; GraphPad Software; computed using trapezoid rule) to estimate the patient specific dose delivered to the blood for the first 24 h of each treatment cycle. As less than 1% of the activity remains at 24 h post-irradiation, it was assumed that the additional dose deposited from 24 h to $t = \infty$ was negligible. The uncertainty on the $^{223}$Ra absorbed blood dose estimates was dominated by the uncertainty in the amount of circulating $^{223}$Ra at each time period, which, as discussed below, could be up to 50% [39–41].

*2.1.2. IMRT blood flow model*

For this part of the work, data was assessed from 13 ADDRAD patients, for whom treatment plan and patient specific data were available. The blood flow model (BF) enabled estimation of dose within the high dose organ area. The absorbed blood dose per fraction ($D_B$) was estimated as follows:

$$D_B = D_f\ (V_{95} \div V_B) \tag{1}$$

where $D_B$ was absorbed dose to blood per fraction, $D_f$ was the prescribed dose per fraction, $V_{95}$ represents the high dose volume and $V_B$ was the total blood volume.

Two variates of the model were used: $BF_1$, which was applied as per Moquet et al. [32] which estimates $V_B$ by assuming 75 ml of blood per kg and, $BF_2$ which uses the static volume of blood in the prostate and lymph nodes for $V_B$, estimated by calculating a scaling factor between the whole-body volume and the area irradiated (prostate and/or lymph nodes) on the basis of treatment plan information. This scaling factor was then applied to the whole-body blood volume estimates to achieve a static blood volume for prostate and lymph nodes. In both cases, $D_F$ and $V_{95}$ were taken from the treatment plans. The uncertainty on $V_B$ and $V_{95}$ was estimated to be on the order of 10%, and the uncertainty on $D_f$ can be estimated on the basis of Moquet and colleagues to be up to 20%. Hence a conservative estimate of uncertainty on $D_B$ would be approximately ±25%.

*2.1.3. IMRT CT plan model*

For this part of the work, data from 13 ADDRAD patients was assessed, for whom treatment plan and patient specific data were available. The CT planned volume (CTPV) absorbed blood dose model enables dose estimation of both high and low dose areas. The CT volume mapped for each patient was utilized to calculate a scaling factor for each patient relative to whole-body volume, with whole-body volume being calculated based on the average patient weight (kg) over the course of treatment [44]. For the following dose models, the whole CT volume was considered within the $CTPV_1$ along with a high dose volume only $CTPV_2$. Utilizing the $CTPV_1$ model, the whole-body mean dose was estimated, and it was assumed the blood volume had also received this. Firstly, a scaling factor, S, was estimated as the ratio between the CT plan volume and the whole-body volume. The following was then applied to estimate the absorbed blood dose per fraction:

$$D_B = (D_{PB} \div N_F) \div S \tag{2}$$

where $D_B$ was the absorbed dose to blood per fraction; $D_{PB}$ was the mean dose in Gy to the body volume covered by the CT scan (specific to each patient, taken from the treatment plans), $N_F$ was the number of fractions of radiotherapy and S was the patient specific scaling factor. A further estimate, $CTPV_2$, was performed in the same manner but in this case firstly calculating the average dose per fraction for prostate and lymph nodes, and then calculating a scaling factor based on their volume compared to the whole-body volume.

The error associated with the plan volume was considered to be on the order of 1–1.5%. The clinical upper acceptable limit in dose delivery to the treatment plan was within 3%, as anything greater than this would trigger re-calibration of dose planned area. The scaling factor was estimated from whole body volume which was estimated by assuming that 1.01 g of human body mass fits within 1 cm$^3$ and that the tissue density within the target volume was consistent with this for the scaling factor estimation, with an error within 1%. The total error associated with CTPV estimations was considered to be within ±6%.

*2.2. M-FISH dicentric quantification*

*2.2.1. Sample collection*

Whole blood was received from 5 male patients recruited onto the ADRADD trial (EudraCT 2014-00273-39) with full informed consent (NHS REC 15/NI/0074) at The Belfast Health and Social Care Trust. Blood samples were drawn into lithium heparinised anticoagulant tubes, once every 4 weeks, immediately prior to the first (C1) and then within 24 h prior to each subsequent (C2–C5) [$^{223}$Ra]$RaCl_2$ administration (Fig. 1). The samples were then shipped at room temperature for next day delivery to Brunel University London. Upon arrival, the samples were processed and whole blood stimulated to divide to enable the collection of 1st *in vitro* cell division metaphase cells for cytogenetic assessment, as described below.

*2.2.2. Cell culture*

For each sample, 0.4 ml of whole blood was used to inoculate 2.6 ml of freshly prepared media (PBMAX Karyotyping Medium) (ThermoFisher, Cat. Number 12557021) supplemented with 0.5 μg/ml purified phytohaemagglutinin (PHA) (ThermoFisher, Cat. Number R30852801), 10 μM 5-bromo-2′-deoxyuridine (BrdU, Sigma-Aldrich Cat. Number 19-160), 10 μl/ml heparin (Sigma-Aldrich Cat. Number 9041-08-1) and cultured in a humidified incubator at 37 °C (95% air/5% $CO_2$), at a 45° angle, and with the cap left slightly open to allow gaseous exchange. Cultures were set up to maximise the yield of 1st cell division of peripheral blood lymphocytes (PBLs) and harvested using standard cytogenetic techniques after a total of 50–60 h. To arrest cells at the metaphase stage of the cell cycle, 50 μl/ml of Colcemid KaryoMAX (ThermoFisher, Cat. Number 1521012), a tubulin inhibitor, was added 4 h prior to harvest. After this time, the cultures were centrifuged at 200*g* for 10 min and the cell pellet re-suspended before the addition of 0.075 M KCl hypotonic solution (Fisher Scientific Cat Number10575090) for 8 min at 37 °C. Cells were then centrifuged at

200g for 10 min and fixed in 3:1 methanol (Thermo Fisher Catalogue Number 15654570) acetic acid (Thermo Fisher Catalogue Number 1743468) on ice. The fixation process was repeated until the samples appeared clear (~5 times), and these were then stored in the freezer at −20 °C.

*2.2.3. Harlequin stain*

Fixed chromosome preparations were dropped onto clean, grease-free slides and assessed for metaphase quality. Harlequin staining was used to assess the number of 1st division metaphase cells. For this, slides were aged on a hot plate for 45 min at 90 °C and immersed in Hoescht (Thermo Fisher Scientific Cat Number 62249) for 10 min, then transferred to a flat tray and covered in 2× Saline-Sodium Citrate (SSC) (Thermo Fisher Cat Number 15557036), before being exposed in UV box to 1.0 J/cm$^2$ for 1 h. After exposure slides were washed with distilled water twice and air dried. Treated slides were stained in 5% Giemsa (VWR Cat Number 350864) for 4 min, removed and rinsed with distilled water. Once dry, the slides were mounted with coverslips with 4 drops of DPX (Fisher Scientific Cat Number 15538321). Slides were scored using brightfield microscopy with oil immersion at ×100 magnification. The fraction of 1st/2nd/3rd division cells was determined based upon the chromatid staining patterns [45,46]. Samples with ≤5% 2nd division cells were assayed by M-FISH.

*2.2.4. Multiplex fluorescence in situ hybridisation (M-FISH)*

M-FISH was carried out utilizing 24XCyte staining probe (Metasystems Probe Cat NumD-0125-600-DI) as per manufacturer protocol. Patient slides were selected from 5 patients according to metaphase spread quality and whether samples containing ≤5% 2nd division cells, a minimum of 3 patient slides were painted per cycle. In brief, slides were incubated in 2xSSC at 70 °C (±1 °C) for 30 min. After this time, the cooled slide was transferred into 0.1xSSC at RT for 1 min. Chromosomes were then denatured in 0.07 NaOH at RT for 1 min followed by 1 min incubation in 0.1xSSC, followed by 2xSSC at 4 °C, and then dehydrated through immersion in a series of alcohol solutions of ascending strength (70%, 95% and 100%). The 24Xcyte probe was denatured by incubating at 75 °C (±1 °C) for 5 min, placed on ice briefly and then incubated at 37 °C for 30 min. The probe was overlaid on to the slide and left to hybridize in a humidified chamber at 37 °C (± 1 °C) for 2–3 days. Slides were washed in 0.4xSSC preheated to 72 °C (±1 °C) for 2 min then incubated in 2xSSCT (containing 0.05% Tween20) for 30 s. For counterstaining, the slide was rinsed in double distilled water and left to air dry before application of DAPI/antifade and sealing.

Slides were visualised utilizing 8-position Zeiss Axioplan 2 microscope containing individual filter sets for 24XCyte probe cocktail plus DAPI (FITC, Spectrum Orange, Texas red, Cy5, DEAC and DAPI). Metaphase cells were imaged under x63 oil immersion and captured by Cool Cube driven by Metafer4 version 3.14.191 software. The image files were exported and karyotyped in ISIS version 5.8.11.

*2.2.5. Chromosome aberration classification*

A cell was classified as being apparently normal if all 46 chromosomes were present and contained the appropriate fluorophore combination along their entire length. Only metaphase cells with good fluorochrome staining were selected for analysis in cells containing ≥43 chromosomes. Chromosomal aberrations were identified by colour junctions along the length of each individual chromosome and/or by the presence of chromosomal fragments (Fig. 2b). A chromosome interchange involving 2 breaks in 2 chromosomes was categorised as a simple exchange, and further classified as a reciprocal translocation or dicentric. Ring chromosomes, which involve 2 breaks in one chromosome were also classed as simple [47]. Exchanges involving 3 or more breaks in 2 or more chromosomes were classed as complex and assigned the minimal number of breaks, arms and breaks involved (CAB) [48]. Chromosomes having breaks only, not involving any additional chromosomes, were classed as chromosome breaks. When classifying cells with multiple aberrations, all aberrations were recorded as independent events and the chromosomes involved identified. Where homologous chromosomes were involved, efforts were made to establish whether the homologues were in the same event or in different independent events, mainly by consideration of chromosome length [49]. All exchanges were recorded as either complete (all break-ends re-joined), true incomplete (where one or more break-ends fail to find an exchange partner) or one-way (where one or more elements appear to be missing) [50,51]. The potential transmissibility of exchanges was also recorded, where a stable (transmissible) exchange was defined as complete and with no evidence of unstable elements e.g. dicentric or acentric fragments. Each independent complex event was also determined to be transmissible or non-transmissible and the presence of insertion-type rearrangements were noted [49]. Metaphase spreads were categorised as stable only if all the exchange events detected within that spread were classified as stable. Unstable complex chromosomal exchanges containing polycentric chromosomes were broken down in to their dicentric equivalents whereby each additional centromere within a chromosome structure constituted a dicentric equivalent (dicentric equivalent event = n centromere − 1) (Fig. 2).

*2.3. M-FISH dicentric assay dose estimation*

*2.3.1. Mixed field absorbed blood dose ratio*

For this part of the work, M-FISH analysis was carried out $n = 5$ individuals with a minimum of $n = 3$ patient samples processed for C2–C5. The $^{223}$Ra:IMRT ratio was estimated in two ways. Firstly, by physical

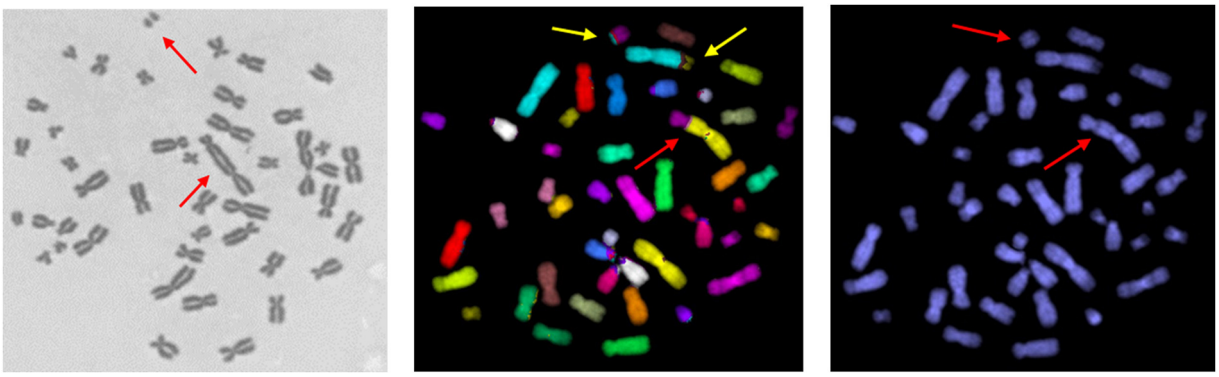

**Fig. 2.** Dicentric equivalent scoring. a) 1st division Giemsa stained metaphase imaged under bright field microscopy ×100 magnification under oil. Chromosome with two centromeres highlighted along with acentric fragment b) Pseudo colour processed image painted by M-FISH, captured at ×63 magnification under oil. Complex chromosomal exchange between three chromosomes, dicentric chromosome highlighted by red arrow along with other components in yellow. c) DAPI channel of same cell (b) highlighting same aberration as a simple dicentric exchange.

dose estimation and secondly, from categorising cells based on the complexity of chromosome exchange observed. For the physical dose ratio, the absorbed blood dose was calculated independently for [$^{223}$Ra]$RaCl_2$ and IMRT (Section 2.1) for each exposure and was summed over the 4-week time period prior to each sample being taken. The average absorbed blood dose per cycle was estimated by averaging the absorbed blood dose across all 13 patients for all treatment cycles. For the dose ratio the overall treatment plan was used (Fig. 1), not the patient specific plan adaptation. Therefore, C2 relates to the response to one injection of [$^{223}$Ra]$RaCl_2$ and 20 IMRT fractions, C3 relates to two injections of [$^{223}$Ra]$RaCl_2$ and 37 IMRT fractions, with C4 and C5 each including the additional [$^{223}$Ra]$RaCl_2$ only administrations. Summing these gives the total absorbed blood dose of [$^{223}$Ra]$RaCl_2$ and IMRT delivered at each time point from C2 to C5. For the M-FISH derived ratio ($M\text{-}FISH_{LET}$), cells containing at least one complex chromosome exchange were classed as being damaged by the traversal of high-LET α-particles from the $^{223}$Ra while cells containing only simple chromosome exchanges, as from IMRT (Section 2.2.5). The ratio of cells containing at least one complex chromosome exchange to cells containing simple exchanges only was therefore a pseudo ratio for $^{223}$Ra:IMRT absorbed blood dose at each cycle point.

#### 2.3.2. Dicentric absorbed blood dose estimation

The dicentric assay traditionally utilizes Giemsa staining where chromosomes are evenly stained in one colour, (Fig. 2a), thus enabling the identification of chromosomes containing more than one centromere along with any associated acentric fragment. In this study, dicentrics were quantified from M-FISH painted metaphase cells (Fig. 2b and c).

Dose estimation was first carried out utilizing the dicentric equivalent frequency as determined by M-FISH. For the IMRT, the $^{60}$Co calibration curve of Lloyd and colleagues, 1986, was used [52] where whole blood was irradiated *in vitro* utilizing a $^{60}$Co source with dose range of 0–5 Gy. The dicentric yield was entered into Dose Estimate V5.2 [53] with the following coefficients $\alpha = 0.0756 \pm 0.0031$, $\beta = 0.0149 \pm 0.0060$ and $C = 0.0004 \pm 0.0009$ [52]. This being a well-established calibration curve, it has been utilized in many exposure scenarios for γ-ray and X-ray dose estimation by Public Heath England and was judged to be the most comparable curve in terms of type and energy of radiation exposure. As there is currently no $^{223}$Ra calibration data, a calibration curve based on a $^{239}$Pu, which emits α-particles of a similar energy to $^{223}$Ra (5.16 MeV per α-particle), was selected. The $^{239}$Pu calibration curve of Purrott et al. [54] was used, the curve coefficients were: $\beta = 0.3696 \pm 0.0322$, $C = 0.0019 \pm 0.0126$ [54]. The decay chain of $^{223}$Ra and $^{239}$Pu does differ, however, due to the perceived lack of risk of a radiation accident involving alpha exposures and the complexity of the experiments, alpha curves for biodosimetry are rare. This curve was established by irradiating whole blood with $^{239}$Pu in the range of 0–1.6 Gy. It is important to note, however, that in this study, the likely non-homogeneous, partial body, nature of both the $^{223}$Ra and IMRT exposures beyond the treatment plan details, was not further considered, neither was the microdosimetric heterogeneity of radium in areas of high bone turnover, and thus this represents a key source of unquantified uncertainty. This aspect will need to be incorporated into further development of absorbed blood dose models. To calculate the absorbed blood dose in this mixed exposure scenario, the "criticality" model was used [35]. In brief, all aberrations were firstly assumed to be attributed to $^{223}$Ra and from the dicentric equivalent yield the dose was estimated. The absorbed blood dose ratio ($^{223}$Ra:IMRT) calculated according to Section 2.3.1. was then used to estimate the IMRT dose and then the gamma calibration curve used to estimate the dicentric equivalent yield. This IMRT yield was then subtracted from the total yield to give a 'new' $^{223}$Ra dicentric equivalent yield. This iterative process was repeated until self-consistent estimates were obtained.

### 2.4. Other statistical analysis

Statistical analysis was performed using GraphPad Prism 9 (GraphPad Software). Descriptive statistics are presented as mean ± SE for pooled data. Standard propagation of errors was applied to estimate the uncertainty in the derived dose estimates. Normality testing indicated ANOVA was appropriate in order to test for differences in aberration frequencies between treatment rounds and for differences in estimated doses.

## 3. Results

### 3.1. Estimating the blood dose from the treatment schedule

Patient data related to the planned treatment for 13 patients was available for physical dose estimation. Table 1 gives the absorbed blood dose per fraction predicted by the BF model, estimated for each patient for the prostate, lymph nodes, and total high dose region combined. The majority of the absorbed blood dose was estimated as being from lymph node exposure, due to the larger volume of irradiation for this tissue ($BF_1$). The total prostate-only absorbed blood dose was found to be in the range of 0.880–1.962 Gy by the end of IMRT treatment (30–37 fractions; 37 fractions assumed for dose ratio calculations in Section 3.3), comparable to the 0.38–1.92 Gy reported by Moquet et al. To consider the differences in lymphatic fluid shift, the static volume was calculated ($BF_2$) and, by combining the BF models ($BF_{1P} + BF_{2\text{-}LN}$), the cumulative absorbed blood dose was estimated to be between 1.131 and 2.717 Gy.

The absorbed blood dose was estimated for the whole CT plan area, including high dose and low dose regions ($CTPV_1$) and for high dose regions only ($CTPV_2$) to enable comparison with the BF model.

Previous CTPV approaches have used a fixed scaling factor of 2.5 with a reported uncertainty of 20%. In this work we instead estimated a patient specific scaling factor between 2.08 and 2.64, with the largest deviation from the scaling factor for Patient 10 being 16% smaller than the published 2.5 scaling factor. The increased absorbed blood dose CTPV estimates compared to the BF estimates observed here are likely to be reflective of the large lymph node irradiation volume [32]. To compare the BF and CTPV models, CTPV was also calculated using the high dose volumes of prostate and lymph nodes, termed as $CTPV_2$. To do so, a scaling factor for each component as detailed for $BF_2$, was used. The resulting absorbed blood doses for $CTPV_2$ were found to be comparable to that of $BF_2$ within the uncertainty estimates (Table 2). The average

**Table 1**
BF model. $V_B$ blood volume, $D_B$ blood dose per fraction. $BF_{1P}$ from $BF_1$ prostate dose combined with $BF_2$ LN dose ($BF_{2LN}$). Patients for whom treatment plan and patient specific data were available $n = 13$. Reported estimated uncertainty of 25% for all BF model variants.

| Patient ID | $V_B$ body (ml) | $V_B$ prostate (ml) | $V_B$ LN (ml) | $BF_1$ | | | $BF_2$ | $BF_{1P} + BF_{2LN}$ |
|---|---|---|---|---|---|---|---|---|
| | | | | Prostate $D_B$ (Gy) | LN $D_B$ (Gy) | Total dose $D_B$ (Gy) | LN $D_B$ (Gy) | Total dose $D_B$ (Gy) |
| 1 | 9030 | 12.9 | 54.5 | 0.038 | 0.132 | 0.170 | 0.007 | 0.045 |
| 2 | 7615 | 11.7 | 56.8 | 0.041 | 0.164 | 0.205 | 0.010 | 0.050 |
| 3 | 6288 | 9.5 | 49.2 | 0.040 | 0.171 | 0.212 | 0.009 | 0.049 |
| 4 | 6560 | 12.2 | 57.2 | 0.060 | 0.231 | 0.291 | 0.014 | 0.073 |
| 5 | 6461 | 13.8 | 63.9 | 0.056 | 0.209 | 0.265 | 0.015 | 0.071 |
| 6 | 6985 | 10.8 | 58.9 | 0.041 | 0.184 | 0.225 | 0.011 | 0.052 |
| 7 | 7650 | 9.4 | 52.0 | 0.033 | 0.149 | 0.181 | 0.008 | 0.040 |
| 8 | 5700 | 7.0 | 32.4 | 0.032 | 0.124 | 0.157 | 0.004 | 0.037 |
| 9 | 6290 | 11.5 | 49.1 | 0.050 | 0.154 | 0.204 | 0.007 | 0.058 |
| 10 | 6629 | 14.0 | 52.3 | 0.056 | 0.171 | 0.227 | 0.009 | 0.065 |
| 11 | 5559 | 9.1 | 48.4 | 0.043 | 0.188 | 0.231 | 0.009 | 0.052 |
| 12 | 7883 | 7.1 | 49.2 | 0.024 | 0.135 | 0.159 | 0.007 | 0.031 |
| 13 | 6486 | 10.2 | 54.8 | 0.042 | 0.161 | 0.203 | 0.009 | 0.051 |

**Table 2**
Physically derived absorbed blood dose, in Gy. $^{223}$Ra absorbed blood dose was representative of an average dose to the blood during localization period. The absorbed blood dose after all treatment cycles was calculated for $n = 6$ injections with the exception of Patient 5 where $n = 5$. IMRT absorbed blood dose estimated for whole CT plan area $CTPV_1$ and high dose regions only $CTPV_2$. Scaling factor estimated from patient body volume derived from average weight during treatment. Patient numbers $n = 13$ patients for whom treatment plan and patient specific data were available. Uncertainties of up to 6% for CTPV models and up to 50% considered for the $^{223}$Ra estimates.

| Patient ID | $^{223}$Ra | IMRT | |
|---|---|---|---|
| | $D_B$ (Gy) | $CTPV_1$ $D_B$ (Gy) | $CTPV_2$ $D_B$ dose (Gy) |
| 1 | 0.0116 | 0.105 | 0.013 |
| 2 | 0.0114 | 0.104 | 0.015 |
| 3 | 0.0116 | 0.101 | 0.016 |
| 4 | 0.0118 | 0.113 | 0.022 |
| 5 | 0.0116 | 0.100 | 0.020 |
| 6 | 0.0116 | 0.112 | 0.017 |
| 7 | 0.0117 | 0.092 | 0.014 |
| 8 | 0.0118 | 0.095 | 0.012 |
| 9 | 0.0117 | 0.089 | 0.015 |
| 10 | 0.0115 | 0.113 | 0.017 |
| 11 | 0.0114 | 0.108 | 0.018 |
| 12 | 0.0116 | 0.094 | 0.012 |
| 13 | 0.0114 | 0.088 | 0.015 |

absorbed blood dose per fraction of IMRT was estimated as 0.101 Gy for $CTPV_1$ and 0.016 Gy for $CTPV_2$ (average $n = 13$ patients), each with an estimated uncertainty on the order of 6%.

$BF_1$ and $CTPV_1$ cannot be directly compared as they use different irradiation volumes. The $BF_1$ model assumes the blood flow within prostate and lymph node regions was identical and in doing so, it appears to significantly overestimate the lymph node blood volume. On the basis of this and the simple nature of the other model assumptions, this method likely has the largest uncertainty. Accordingly, only $CTPV_1$ and $CTPV_2$ are considered further as these models represent an estimate of combined absorbed blood dose for high dose regions and low dose regions ($CTPV_1$) and high dose regions only ($CTPV_2$). Supplementary Table 1 details the patient specific injected activities and CT planning volumes. Table 2 shows the individual absorbed blood dose estimates for each $^{223}$Ra administration, and the IMRT absorbed blood dose estimates for each fraction. The average $^{223}$Ra absorbed blood dose per treatment cycle was 0.012 ± 0.002 Gy. The estimated $^{223}$Ra absorbed blood dose per fraction was not found to be statistically different between patients ($P = 0.097$). To estimate the $^{223}$Ra absorbed blood dose per treatment cycle, the median values of the activity kinetics reported in the literature were utilized. Based on the highest and lowest limits reported for each timepoint the $^{223}$Ra blood dose estimates per treatment cycle could vary by up to 50%. This value being reported as a conservative estimate of uncertainty for dose estimates, with more work needed to quantify the variations between patient clearance.

### 3.2. Frequency and type of chromosome aberration in ADRADD patients

M-FISH analysis was carried out on blood samples received from 5 patients for C1–C5. The control samples of all 5 patients were analysed and following this a minimum of 3 patients were analysed per treatment cycle. The background frequency of chromosomal aberrations was found to be within the expected normal range for individuals in the 50+ age bracket [55,56]. Specifically, frequencies of 0.0, 0.024 ± 0.011 and 0.020 ± 0.009 were observed for simple dicentrics, reciprocal translocations and break-only aberrations, respectively (sample C1; pooled for 5 patients). One cell containing an unstable complex rearrangement was found in Patient 2 (0.004 ± 0.004), for which the origin was not clear.

Simple chromosomal exchanges were observed to significantly increase in frequency between C1 and C2 (0.024 ± 0.011 to 0.319 ± 0.042 ($P < 0.001$)) and further at C3 to 0.484 ± 0.042 ($P < 0.031$) (Supplementary Table 2). No other statistical differences were noted between treatment cycles (C3–4, $P = 0.966$ or C4–C5, $P = 0.996$), suggesting the majority of simple aberrations formed early in the treatment regime persist over the period sampled, and/or the induction of new aberrations was balanced by cell death of unstable (e.g. dicentric) types. The frequency of complex exchanges increased from 0.058 ± 0.016 at C2 to 0.174 ± 0.022 at C3 ($P = 0.007$), rising further to 0.265 ± 0.037 at C4 and 0.210 ± 0.030 at C5 (Supplementary Table 2).

In terms of classification of complexity, the frequency of damaged PBLs assigned to each exposure type ($^{223}$Ra or IMRT) was reported in Fig. 3 and Table 3. This categorisation was based upon the presence or absence of a complex chromosome exchange and shows that the majority of damaged PBLs sampled, with combined IMRT and $^{223}$Ra contained mostly simple exchanges only at C2 (cells containing simple exchanges 0.204 ± 0.025 and containing at least one complex exchange 0.050 ± 0.014, $P < 0.001$) and C3 (0.243 ± 0.021 and 0.150 ± 0.018, $P = 0.006$). After this time, when patients continue to receive $^{223}$Ra only, the fraction of damaged PBLs with at least one complex exchange increased. In the $^{223}$Ra only cycles, no significant difference between cells containing a simple aberration and those containing at least one complex exchange was observed (C4 $P = 0.992$, C5 $P = 0.558$).

### 3.3. M-FISH dicentric assay absorbed blood dose estimates

The absorbed blood dose ratios were estimated for C2–C5, this was equivalent to 4 intravenous injections of $^{223}$Ra and completed IMRT schedule of 37 fractions by C5. For the physical dose ratio, this was based on the average absorbed blood dose per fraction across all 13 patients for both the IMRT and $^{223}$Ra dose. The M-$FISH_{LET}$ ratios described in Section 2.3.1, was obtained from blood samples received from 5 patients with a minimum of 3 patient samples analysed per cycle. The absorbed blood dose ratios for all models can be seen in Table 3. Applying these blood dose ratios to the dicentric assay, the absorbed blood dose was estimated in three ways (Table 4). The CTPV methods were derived from the physical absorbed blood dose estimates as per method Section 2.1. with $CTPV_1$ estimating the absorbed blood dose across the planned volume including both high and low dose volumes while $CTPV_2$ including the high dose regions only. The M-$FISH_{LET}$ absorbed blood dose was instead estimated from the ratio of cells consistent with high LET exposure ($^{223}$Ra) and low LET exposure (IMRT).

The absorbed blood dose estimates from the CTPV models suggest the dose after 20 IMRT fractions, measured at C2 (Table 4), was between 1.327 ± 0.115 Gy and 1.395 ± 0.115 Gy. The M-$FISH_{LET}$ method was found to be in similar range at 0.956 ± 0.114 Gy at C2. The IMRT absorbed blood dose after the end of fractionation (C3 assuming 37 completed fractions) was estimated for $CTPV_1$ as 2.148 ± 0.096 Gy and 2.073 ± 0.096 Gy for $CTPV_2$, with M-$FISH_{LET}$ blood dose estimates of 1.167 ± 0.092 Gy.

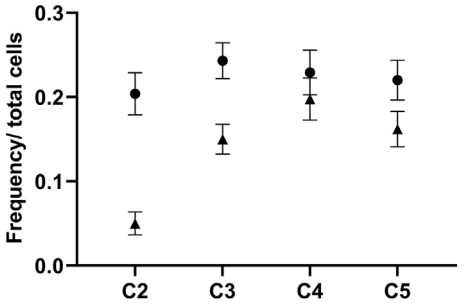


**Fig. 3.** Frequency of cells containing either simple (●) or at least one complex (▲) chromosome exchange. Data pooled from 5 patients total, $n = 3$ patients/cycle (C2, 3 and 5) and $n = 4$ for C3. Error bars represent standard error of the mean for pooled data.

**Table 3**
Absorbed blood dose ratios. M-FISH derived ratio based on the complexity of cellular damage with $^{223}$Ra assigned cells to include those with at least 1 complex exchange and, IMRT assigned cells defined as containing only simple exchanges. Frequency per total cells scored pooled per cycle, with calculated SE. $D_B$ per cycle of patient average ($n = 13$), complexity of cellular damage from pooled patient data ($n = 5$).

| Cycle | Cellular classification | | $D_B$ per cycle | | | $^{223}$Ra: IMRT | | |
|---|---|---|---|---|---|---|---|---|
| | $^{223}$Ra cells (f) | IMRT cells (f) | $^{223}$Ra (Gy) | IMRT CTPV$_1$ (Gy) | IMRT CTPV$_2$ (Gy) | CTPV$_1$ | CTPV$_2$ | M-FISH$_{LET}$ |
| C2 | 0.050 ± 0.014 | 0.204 ± 0.025 | 0.012 ± 0.002 | 2.021 ± 0.050 | 0.318 ± 0.017 | 1:174 | 1:27 | 1:4 |
| C3 | 0.150 ± 0.018 | 0.243 ± 0.021 | 0.023 ± 0.003 | 3.739 ± 0.092 | 0.587 ± 0.031 | 1:161 | 1:25 | 2:3 |
| C4 | 0.198 ± 0.025 | 0.229 ± 0.026 | 0.035 ± 0.003 | 3.739 ± 0.092 | 0.587 ± 0.031 | 1:108 | 1:17 | 1:1 |
| C5 | 0.162 ± 0.021 | 0.220 ± 0.024 | 0.046 ± 0.004 | 3.739 ± 0.092 | 0.587 ± 0.031 | 1:81 | 1:13 | 3:4 |

For the $^{223}$Ra absorbed blood dose at C2, the CTPV$_1$ and CTPV$_2$ were found to be 0.008 ± 0.025 and 0.048 ± 0.032, both lower than the M-FISH$_{LET}$ estimate of 0.150 ± 0.046 Gy. For C3 the $^{223}$Ra absorbed blood dose estimated from CTPV methods was between 0.013 ± 0.025 and 0.082 ± 0.033 Gy (CTPV$_1$ and CTPV$_2$ respectively) with the M-FISH$_{LET}$ absorbed blood dose estimated at 0.719 ± 0.073 Gy. By the final sample point studied here (C5), the absorbed blood dose from $^{223}$Ra was estimated as 0.024 ± 0.027 Gy by CTPV$_1$ and 0.141 ± 0.042 Gy for CTPV$_2$ with the M-FISH$_{LET}$ absorbed blood dose estimate at 0.665 ± 0.080 Gy (see Fig. 4).

## 4. Discussion

In the future, α-particle emitters, such as $^{223}$Ra, alone or in combination, are likely to be adopted in the treatment of a wide range of cancers, contributing to more targeted, personalized medicine with the potential to impact a large number of patients [17,57,58]. To date, however, there are only limited studies using biological endpoints which seek to understand the biological action of $^{223}$Ra *in vivo* in humans, to improve the optimal delivery of these and, to minimise the risk of adverse effects through radiation exposure of normal tissues [59–63]. Quantifying the absorbed blood dose delivered from the treatment is an important step in maximising clinical efficacy and evaluating radiation risks, estimates of which are currently based on population studies [31]. In this study, whole blood was sampled from patients recruited onto the ADRRAD trial [37]. The treatment includes a planned mixed field exposure from daily IMRT fractions, 37 × 2 Gy to prostate with concomitant boost (37 × 1.6 Gy) to lymph nodes, over a period of 7.5 weeks, together with 6 intravenous injections of [$^{223}$Ra]RaCl$_2$ over a period of 20 weeks.

Dose estimation for non-targeted tissues in mixed exposure scenarios is challenging. To account for the mixed field nature of the treatment, existing models were used to determine the ratio of the component radiation types. Additionally, a new approach (M-FISH$_{LET}$), based on the ratio of cells containing damage consistent with high-LET exposure (complex chromosomal exchanges) and low-LET exposure (simple exchanges), was used as a pseudo ratio for $^{223}$Ra:IMRT absorbed blood dose.

$^{223}$Ra exposure was dictated by its unique pharmacokinetic properties and its ability to target calcium-dependent bone turnover. Once intravenously administered, $^{223}$Ra is rapidly cleared through the gastrointestinal tract and the remainder through the kidneys [39,41]. Previous studies on rodents found minimal uptake of $^{223}$Ra in non-targeted areas such as kidneys and the spleen [13,64] with the highest absorbed doses being observed in humans in neighbouring sites of target bone metastases, including osteogenic cells and the red bone marrow [17,19,20]. Here, the $^{223}$Ra absorbed blood dose was estimated from the injected activity using an existing clearance model, based on the quantity of $^{223}$Ra in circulation at three time points (15 min, 4 h and 24 h post intravenous administration). The uncertainty for the $^{223}$Ra physical absorbed blood dose estimations per cycle was based on the errors associated with the injected activity, patient weight and clearance models used. The injected activity per patient was estimated from the known activity in the syringe prior to administration and the remaining activity after injection, the error associated with this was considered negligible. Patient individual weights were found to fluctuate during treatment by 8% (up to 6.2 kg lost by C6). Therefore, the $^{223}$Ra absorbed blood dose was estimated for each chosen timepoint from the data available at the specific treatment cycle rather than an average across treatment

**Table 4**
Absorbed blood doses during treatment (Gy) calculated on the basis of CTPV$_1$, CTPV$_2$ and M-FISH$_{LET}$ models. Patients sampled during treatment cycles were coded and identifier number (ID) assigned, $n = 5$ patients were assayed by M-FISH to determine the dicentric equivalent yield. The absorbed blood dose was calculated with use of dicentric assay for each patient with the dose ratios estimated from CT plan and M-FISH$_{LET}$ derived models. The SE was reported for the absorbed blood dose estimation, this being the largest uncertainty for M-FISH$_{LET}$ dose estimation. CTPV$_1$ and CTPV$_2$ reported SE of absorbed blood dose estimation with a propagated conservative uncertainty estimated up to 50% not included.

| Cycle | Patient ID | Cells scored | Dicentric equivalents (yield ± SE) | | CTPV$_1$ | | CTPV$_2$ | | M-FISH$_{LET}$ | |
|---|---|---|---|---|---|---|---|---|---|---|
| | | | | | $^{223}$Ra | IMRT | $^{223}$Ra | IMRT | $^{223}$Ra | IMRT |
| 2 | 1 | 55 | 8 | (0.145 ± 0.066) | 0.007 ± 0.033 | 1.268 ± 0.246 | 0.044 ± 0.054 | 1.201 ± 0.246 | 0.207 ± 0.105 | 0.845 ± 0.245 |
| | 3 | 101 | 16 | (0.158 ± 0.067) | 0.008 ± 0.029 | 1.329 ± 0.182 | 0.046 ± 0.043 | 1.261 ± 0.182 | 0.221 ± 0.081 | 0.899 ± 0.181 |
| | 4 | 104 | 21 | (0.202 ± 0.048) | 0.009 ± 0.029 | 1.516 ± 0.180 | 0.053 ± 0.045 | 1.448 ± 0.180 | 0.263 ± 0.086 | 1.070 ± 0.179 |
| | Total | 260 | 45 | (0.173 ± 0.035) | 0.008 ± 0.025 | 1.395 ± 0.115 | 0.048 ± 0.032 | 1.327 ± 0.115 | 0.235 ± 0.055 | 0.959 ± 0.114 |
| 3 | 1 | 100 | 30 | (0.30 ± 0.0820) | 0.012 ± 0.031 | 1.874 ± 0.184 | 0.071 ± 0.051 | 1.799 ± 0.184 | 0.584 ± 0.128 | 0.947 ± 0.182 |
| | 2 | 101 | 38 | (0.376 ± 0.076) | 0.013 ± 0.031 | 2.113 ± 0.184 | 0.080 ± 0.053 | 2.038 ± 0.184 | 0.701 ± 0.139 | 1.138 ± 0.182 |
| | 4 | 101 | 45 | (0.446 ± 0.111) | 0.014 ± 0.032 | 2.310 ± 0.185 | 0.088 ± 0.055 | 2.234 ± 0.184 | 0.801 ± 0.149 | 1.300 ± 0.182 |
| | 5 | 105 | 45 | (0.429 ± 0.065) | 0.014 ± 0.031 | 2.264 ± 0.181 | 0.086 ± 0.053 | 2.188 ± 0.181 | 0.777 ± 0.144 | 1.261 ± 0.179 |
| | Total | 407 | 158 | (0.388 ± 0.042) | 0.013 ± 0.025 | 2.148 ± 0.096 | 0.082 ± 0.033 | 2.073 ± 0.096 | 0.719 ± 0.073 | 1.167 ± 0.092 |
| 4 | 1 | 48 | 15 | (0.313 ± 0.099) | 0.018 ± 0.042 | 1.908 ± 0.264 | 0.106 ± 0.082 | 1.797 ± 0.264 | 0.680 ± 0.198 | 0.789 ± 0.262 |
| | 2 | 102 | 53 | (0.520 ± 0.062) | 0.023 ± 0.035 | 2.497 ± 0.184 | 0.141 ± 0.066 | 2.384 ± 0.184 | 1.048 ± 0.169 | 1.216 ± 0.181 |
| | 3 | 103 | 32 | (0.311 ± 0.116) | 0.018 ± 0.033 | 1.902 ± 0.182 | 0.106 ± 0.058 | 1.791 ± 0.182 | 0.677 ± 0.136 | 0.785 ± 0.179 |
| | Total | 253 | 100 | (0.395 ± 0.052) | 0.020 ± 0.028 | 2.162 ± 0.119 | 0.121 ± 0.043 | 2.050 ± 0.119 | 0.833 ± 0.097 | 0.966 ± 0.116 |
| 5 | 1 | 106 | 47 | (0.443 ± 0.083) | 0.028 ± 0.037 | 2.290 ± 0.180 | 0.169 ± 0.070 | 2.142 ± 0.180 | 0.864 ± 0.151 | 1.175 ± 0.178 |
| | 4 | 101 | 35 | (0.347 ± 0.084) | 0.025 ± 0.036 | 2.009 ± 0.184 | 0.147 ± 0.068 | 1.862 ± 0.183 | 0.705 ± 0.140 | 0.959 ± 0.182 |
| | 5 | 102 | 18 | (0.176 ± 0.043) | 0.017 ± 0.033 | 1.394 ± 0.182 | 0.099 ± 0.057 | 1.254 ± 0.181 | 0.392 ± 0.105 | 0.533 ± 0.180 |
| | Total | 309 | 100 | (0.324 ± 0.042) | 0.024 ± 0.027 | 1.937 ± 0.108 | 0.141 ± 0.042 | 1.791 ± 0.108 | 0.665 ± 0.080 | 0.905 ± 0.105 |

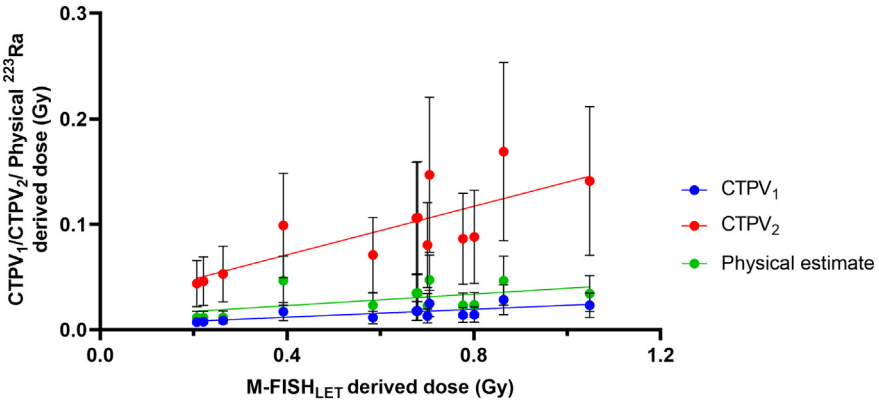


**Fig. 4.** Comparison of $^{223}$Ra dose estimates. M-FISH$_{LET}$ ratio was implemented in the dicentric assay estimates of blood dose for $n = 5$ patients (patient ID 1–5), the estimates for these patients were compared across all other models. CTPV$_1$ and CTPV$_2$ calculated from the dicentric assay utilizing the physical blood dose estimates by $^{223}$Ra and respective IMRT models. Simple linear regression plotted for CTPV$_1$ $Y = 0.019 * X + 0.004$, $R^2 = 0.559$ and for CTPV$_2$ $Y = 0.115 * X + 0.025$, $R^2 = 0.600$. Physical $^{223}$Ra dose estimated through clearance of $^{223}$Ra from circulation 24 h post administration. Simple linear regression plotted for $Y = 0.028 * X + 0.012$, $R^2 = 0.301$. The error associated with the physical $^{223}$Ra was conservatively estimated to 50% and propagated to CTPV$_1$, CTPV$_2$. The error for M-FISH$_{LET}$ dose was propagated as 30% for C2 and 14% for C3–C5.

along with the median values of $^{223}$Ra in the blood at each timepoint (averaged between reported studies). The average absorbed blood dose per cycle was estimated as $0.012 \pm 0.002$ Gy (average of Table 2 as per methods Section 2.3.1). In order to estimate the uncertainty for the clearance model, the reported ranges in terms of upper and lower range limits were taken from the literature [39–41] with a variation from the median of up to 50%. The average uncertainty on the delivered $^{223}$Ra activity was thus estimated to be as high as 50%. The additional absorbed blood dose delivered after 24 h period was not considered in this model. Although the additional absorbed blood dose is likely to be within the 50% uncertainty described, it may not be implicitly negligible and does form an additional contribution to the uncertainty not quantified here.

The physical absorbed blood doses reported here are higher than those reported by Stephan et al. using $^{224}$Ra and in a similar range to those reported by Schumann et al. for $^{223}$Ra [65,66]. The decay kinetics and energies of $^{224}$Ra are broadly comparable to those of $^{223}$Ra, however, as Stephan and colleagues report, there are a number of limitations associated with the application of the ICRP 67 model [67], including the lack of information regarding the local distribution of the activity. The aim of the $^{223}$Ra clearance calculations in this work was not to test the ICRP model, rather, to provide a very simple kinetic method for validation of the newly proposed biological absorbed blood dose estimation methods presented. Nevertheless, further work is required to assess the most appropriate means of estimating dose, and this will include re-assessment of more detailed kinetic models including those from ICRP.

IMRT utilizes conformal beams to accurately target a designated area minimising exposure to non-target organs/tissues. Unlike $^{223}$Ra, this treatment is tailored to the disease burden of each patient with the number of fractions, dose and area covered dependent upon patient specific information (Supplementary Table 1). Using this, estimates were carried out employing two models previously described by Moquet and colleagues, which were designed to provide a relatively simple assessment of RT doses [32]. The first model, the blood flow model (BF), was based on the time taken for blood to flow through the high dose planned area. Moquet et al., assumed that 6 L of whole blood flows through the high dose region within a 1-min IMRT exposure time [32]. For this study, individual patient weights were available, therefore blood volume was more accurately estimated by assuming each kg of body weight contains 75 ml of blood [68], (BF$_1$). The absorbed blood dose per fraction was then estimated to range between 0.159 and 0.291 Gy and this was equivalent to a cumulative dose of 5.872–8.715 Gy at IMRT treatment completion (see supplementary Table 1). Although lymph nodes are in proximity of vascularized tissue, they do not circulate blood, instead they circulate lymph fluid. BF$_1$ was therefore likely to overestimate the lymph node absorbed dose. The fluid shift within lymph nodes is approximated to ~4 L per day [69] which may be negligible during treatment. To model the lymph node exposure, the static absorbed blood dose was calculated (BF$_2$) using similar principles, subsequently scaled down to lymph node planned volume. Lymph node absorbed blood dose per fraction represents 0.004–0.015 Gy which was equivalent to 0.152–0.508 Gy by IMRT completion (patient individualised schedule). This BF$_2$ model was likely to be a more accurate representation of static PBL irradiation in this tissue that may then be filtered to the circulatory system. By combining the two models, the cumulative absorbed blood dose to high dose volume likely was between 1.131 and 2.470 Gy by completion of individualised IMRT schedule. Neither of these models consider the low dose regions that are also exposed during treatment; therefore, so both will underestimate the total blood dose. The original work of Moquet and colleagues [32] was relatively simple and requires further validation to ascertain exposure circumstances in which such models can be applied. In this study, patient specific data was utilized to refine these models, with limited success. The uncertainties in CTPV absorbed blood dose were derived by propagation of the uncertainties associated with factors in Eqs. (1) and (2). For CTPV physical absorbed blood dose these were the planned volume (considered minimal at 1–1.5% variation), the dose to planned volume and the estimated scaling factors. The dose to the plan region was expected to have an uncertainty of less than 3%, based on published estimates of the upper bound of inter-treatment dosimetric uncertainty [70] and greater errors would be detected by treatment QA and trigger re-planning and re-validation. To estimate the whole-body volume, it was assumed that 1.01 g of human body mass fits within 1 cm$^3$ and that the tissue density within the target volume was consistent with this for the scaling factor estimation, with an error within 1%. The total error associated with CTPV estimations was considered to be 6%. It is important to note, however, that the estimates of uncertainty are themselves uncertain and further work is needed here to better understand how patient specific data can contribute to such estimates. In addition, more detail with respect to beam-on times are required to improve the BF dose model, in particular, for larger dose volumes, therefore, despite its use previously, this model was not considered further.

To enable the absorbed blood dose estimation by dicentric assay in this mixed ($^{223}$Ra and IMRT) exposure scenario, the absorbed blood dose ratio between each source was estimated per treatment cycle. This then facilitated use of the “criticality” dose estimation technique, originally designed to separate and quantify neutron and gamma exposures following a nuclear accident or incident [35], but here used to assess the IMRT and α-particle absorbed doses, on the basis of either the

treatment planning information (CTPV ratios), or the categorisation of complexity of aberrations observed using M-FISH. The dicentric assay was applied to two separate models, the first utilizing the ratio derived from physical models, $^{223}$Ra clearance and IMRT CTPV models, and the second utilizing the M-FISH$_{LET}$ ratio based on the categorisation of high LET to low LET exposed cells. The absorbed blood dose estimations were carried out for 5 patients for which blood samples were drawn and the dicentric equivalent frequency estimated. The CTPV derived ratios assume that IMRT induced aberrations accumulated in the circulatory blood pool by C3 are not cleared from the peripheral pool in the following C4 and C5 treatment cycles and similarly for the $^{223}$Ra, it was assumed the aberrations accumulate through treatment with no clearance. This results in a plateau of IMRT dose for CTPV$_1$ as the dose ratio was based on a large IMRT component with a small $^{223}$Ra dose. For CTPV$_2$, as the model was based on high dose regions areas, the IMRT estimated dose was lower than CTPV$_1$, therefore when expressed as a ratio with $^{223}$Ra, this assumes a higher proportion of absorbed blood dose to be attributed to $^{223}$Ra, which decreases the estimated dose for C4 and C5. The dicentric assay was estimated from the ratio of physical $^{223}$Ra and CTPV dose estimates with a conservative error of 50% being attributed to the $^{223}$Ra dose, this was considered to be the largest uncertainty. Future studies will aim to reduce this uncertainty by increasing the number of patients in the study and by including later timepoints.

The M-FISH$_{LET}$ model was based on the chromosomal aberration spectrum in PBL sampled 4 weeks after each [$^{223}$Ra]RaCl$_2$ administration. Following IMRT completion, the dose was estimated at 1.167 ± 0.092 Gy. This was based on the assumption that all IMRT induced aberrations would be of simple type while $^{223}$Ra aberrations were of complex type. As a larger proportion of cells containing complex aberrations than simple chromosomal aberrations was observed, this was reflected in the dose ratio. Accordingly, the dose attributed to $^{223}$Ra was proportionally larger than that attributed to IMRT. The resulting IMRT absorbed blood dose estimated by M-FISH$_{LET}$ was therefore lower than both CTPV dose estimates. The physically derived $^{223}$Ra estimates were representative of the period taken for $^{223}$Ra to clear from the blood. Due to the sampling schedule being every 4 weeks, it cannot be excluded that absorbed dose from $^{223}$Ra was also received by circulating PBLs in the vicinity of metastatic sites, especially as metastatic sites tend to be highly vascularized [71–73]. The M-FISH$_{LET}$ absorbed blood dose estimates may better account for this, with the $^{223}$Ra dose by C5 estimated to be 0.665 ± 0.080 Gy. This estimate was significantly larger than CTPV$_1$ 0.024 ± 0.027 Gy and CTPV$_2$ 0.141 ± 0.042 Gy. The largest uncertainty in the M-FISH$_{LET}$ absorbed blood dose estimation was found to be also in C2 whereby the variation in the frequency of cells consistent with IMRT exposure (cells containing simple aberrations only) was up to 13% and for those consistent with $^{223}$Ra exposure of up to 28%. The error from the calibration curve used was estimated to be 12 and 23% for IMRT and $^{223}$Ra absorbed blood dose estimates, respectively. The total propagated error on absorbed dose was within 30% for the M-FISH$_{LET}$ derived estimates.

In this study, the complexity of chromosome exchange observed in PBLs was used as a biomarker of radiation quality [36] from which to make estimates of absorbed blood dose ratio, termed the M-FISH$_{LET}$. Based upon principles of radiation track structure and PBL cell geometry [36,74], all cells which contained at least one complex chromosome exchange [75,76] were categorised as having been traversed by high LET α-particles emitted from the $^{223}$Ra, while damaged cells containing only simple chromosome exchanges (reciprocal translocation, dicentrics and rings) were categorised as being exposed to low LET radiation from IMRT. Although *in vitro* studies do show the majority of high-LET induced damage to result in complex chromosome aberrations largely independent of dose [77–81] it is also the case that the simple exchanges can be directly induced after α-particles of lower incident LET [74] and, exposure to low-LET radiation will result in the formation of complex exchanges, in a manner strongly dependent upon dose [50,82,83]. For instance, an increasing fraction of complex exchanges of up to 20–40% have previously been attributed to exposure of a large target field in IMRT treated prostate cancer patients [84,85]. Therefore, it is likely that IMRT absorbed blood dose may be underestimated using the M-FISH$_{LET}$ reported here. Given the potential usefulness of this ratio in cases of unknown exposures where physical information is not available, further work to determine frequencies of complex exchange occurrence in IMRT only and $^{223}$Ra only treated patients is required.

As the M-FISH$_{LET}$ absorbed dose ratio and the dicentric quantification was based on cytogenetic observations of sampled PBL, the resulting doses estimated will be directly affected by haematopoietic cell death and repopulation dynamics. The IMRT dose estimates were found to plateau between C3–C5 suggesting cells containing unstable aberrations remain over the time course studied. However, IMRT has been shown to significantly decrease the number of PBLs in circulation, and therefore the clearance and repopulation dynamics should also be taken into consideration for the CTPV models [25,86,87]. White blood cell counts have been found to increase within 6–8 weeks of therapy completion with a significant increase in lymphocyte population after 3 months [26,88]. The 4-week period between C3–C4 (after end of IMRT) could provide a sufficient break for haematopoietic cells to boost PBL repopulation, which if the case, would have the effect of diluting the frequency of persisting unstable chromosomal events. Newly induced aberrations by subsequent $^{223}$Ra treatment cycles would then add to this aberrant cell pool. There is also the potential of bystander responses playing a role both in cell turnover and aberration formation [89]. Further work on blood samples representative of later [$^{223}$Ra]RaCl$_2$ administrations (C6) and follow up samples (up to 1 year post start of treatment), together with patient hematological counts, will help elucidate the cellular dynamics of damaged PBL. An assessment of the occurrence and type of stable chromosome exchange from these samples will also offer the potential to make estimates of absorbed dose delivered to the bone marrow.

In conclusion, in this study we have evaluated a number of absorbed blood dose methods for mixed field exposure, in a unique population of patients receiving external beam photons and a systemically delivered α-emitter $^{223}$Ra. We highlight key observations and limitations to establish an approach from which we can make dose assessments to better understand mixed field exposures. The models presented provide an initial estimation of cumulative absorbed dose received to the blood during incremental IMRT fractions and [$^{223}$Ra]RaCl$_2$ injections, all of which move towards assessing patient specific dose information for mixed field treatment to help optimise treatment outcomes and minimise patient risk in the future.

## Acknowledgements

This project received funding from Public Health England, as part of the PHE PhD studentship scheme. This work was supported by the Movember Prostate Cancer UK Centre of Excellence (CEO13_2-004) and the Research and Development Division of the Public Health Agency of NI (COM/4965/14).

## Appendix A. Supplementary data

Supplementary data to this article can be found online at https://doi.org/10.1016/j.nucmedbio.2021.12.002.

## References

[1] Halabi S, Small EJ, Kantoff PW, Kattan MW, Kaplan EB, Dawson NA, et al. Prognostic model for predicting survival in men with hormone-refractory metastatic prostate cancer. J Clin Oncol. 2003;21(7):1232–7. https://doi.org/10.1200/jco.2003.06.100.

[2] Parker C, Finkelstein SE, Michalski JM, O'Sullivan JM, Bruland Ø, Vogelzang NJ, et al. Efficacy and safety of Radium-223 dichloride in symptomatic castration-resistant prostate cancer patients with or without baseline opioid use from the phase 3 ALSYMPCA trial. Eur Urol. 2016;70(5):875–83. https://doi.org/10.1016/j.eururo.2016.06.002.

[3] Parker C, Nilsson S, Heinrich D, Helle SI, O'Sullivan JM, Fosså SD, et al. Alpha emitter radium-223 and survival in metastatic prostate cancer. N Engl J Med. 2013;369(3):213. https://doi.org/10.1056/nejmoa1213755.
[4] Parker C, Heinrich D, O'Sullivan JM, Fossa SD, Chodacki A, Demkow T, et al. Overall survival benefit and safety profile of radium-223 chloride, a first-in-class alpha-pharmaceutical: results from a phase III randomized trial (ALSYMPCA) in patients with castration-resistant prostate cancer (CRPC) with bone metastases. J Clin Oncol. 2012;30(5_suppl):8. https://doi.org/10.1200/jco.2012.30.5_suppl.8.
[5] Xofigo. https://www.ema.europa.eu/en/medicines/human/referrals/xofigo; 2018. [Accessed 17 February 2021]..
[6] Postmarket Drug and Biologic Safety Evaluations. Completed from January 2017 – March 2017. https://www.fda.gov/drugs/surveillance/postmarket-drug-and-biologic-safety-evaluations-completed-january-2017-march-2017; 2017. [Accessed 17 February 2021]..
[7] Nilsson S, Prof Franzén L, MD Parker C, Dr Tyrrell C, FRCR Blom R, MD Tennvall J, Prof. Bone-targeted radium-223 in symptomatic, hormone-refractory prostate cancer: a randomised, multicentre, placebo-controlled phase II study. Lancet Oncol. 2007;8(7):587–94. https://doi.org/10.1016/s1470-2045(07)70147-x.
[8] Nilsson S, Strang P, Aksnes AK, Franzèn L, Olivier P, Pecking A, et al. A randomized, dose–response, multicenter phase II study of radium-223 chloride for the palliation of painful bone metastases in patients with castration-resistant prostate cancer. Eur J Cancer. 2012;48(5):678–86. https://doi.org/10.1016/j.ejca.2011.12.023.
[9] Nickoloff JA, Sharma N, Taylor L. Clustered DNA double-strand breaks: biological effects and relevance to cancer radiotherapy. Genes. 2020;11(1):99 10.3390%2Fgenes11010099.
[10] Bannik K, Madas B, Jarzombek M, Sutter A, Siemeister G, Mumberg D, et al. Radiobiological effects of the alpha emitter ra-223 on tumor cells. Sci Rep. 2019;9(1):1–11. https://doi.org/10.1038/s41598-019-54884-7.
[11] Ritter MA, Tobias CA, Cleaver JE. High-LET radiations induce a large proportion of non-rejoining DNA breaks. Nature. 1977;266(5603):653–5. https://doi.org/10.1038/266653a0.
[12] Nilsson S, Larsen RH, Fosså SD, Balteskard L, Borch KW, Westlin J, et al. First clinical experience with α-emitting Radium-223 in the treatment of skeletal metastases. Clin Cancer Res. 2005;11(12):4451–9. https://doi.org/10.1158/1078-0432.ccr-04-2244.
[13] Henriksen G, Breistøl K, Bruland ØS, Fodstad Ø, Larsen RH. Significant antitumor effect from bone-seeking, alpha-particle-emitting (223)Ra demonstrated in an experimental skeletal metastases model. Cancer Res. 2002;62(11):3120–5.
[14] Pandit-Taskar N, Larson SM, Carrasquillo JA. Bone-seeking radiopharmaceuticals for treatment of osseous metastases, part 1: therapy with 223Ra-dichloride. J Nucl Med. 2013;55(2):268–74. https://doi.org/10.2967/jnumed.112.112482.
[15] Heinrich D, Bektic F, Bergman AM, Caffo O, Cathomas R, Chi KN, et al. The contemporary use of Radium-223 in metastatic castration-resistant prostate cancer. Clin Genitourin Cancer. 2017;16(1):223–31. https://doi.org/10.1016/j.clgc.2017.08.020.
[16] Kerr C. (223)Ra targets skeletal metastases and spares normal tissue. Lancet Oncol. 2002.;453. https://doi.org/10.1016/s1470-2045(02)00835-5 Sect. 3.
[17] Flux GD. Imaging and dosimetry for radium-223: the potential for personalized treatment. Br J Radiol. 2017;90(1077):20160748. https://doi.org/10.1259/bjr.20160748.
[18] Pacilio M, Ventroni G, De Vincentis G, Cassano B, Pellegrini R, Di Castro E, et al. Dosimetry of bone metastases in targeted radionuclide therapy with alpha-emitting (223)Ra-dichloride. Eur J Nucl Med Mol Imaging. 2016;43(1):21–33. https://doi.org/10.1007/s00259-015-3150-2.
[19] Lassmann M, Nosske D. Dosimetry of 223Ra-chloride: dose to normal organs and tissues. Eur J Nucl Med Mol Imaging. 2013;40(2):207–12. https://doi.org/10.1007/s00259-012-2265-y.
[20] Hobbs RF, Song H, Watchman CJ, Bolch WE, Aksnes A, Ramdahl T, et al. A bone marrow toxicity model for 223Ra alpha-emitter radiopharmaceutical therapy. Phys Med Biol. 2012;57(10):3207–22. https://doi.org/10.1088/0031-9155/57/10/3207.
[21] Leung CN, Canter BS, Rajon D, Bäck TA, Fritton JC, Azzam EI, et al. Dose-dependent growth delay of breast cancer xenografts in the bone marrow of mice treated with 223Ra: the role of bystander effects and their potential for therapy. J Nucl Med. 2020;61(1):89–95. https://doi.org/10.2967/jnumed.119.227835.
[22] FDC Guerra-Liberal, O'Sullivan JM, SJ McMahon, Prise KM. Targeted alpha therapy: current clinical applications. 2020;35(6):404–17. https://doi.org/10.1089/cbr.2020.3576 June 16.
[23] Moghaddam FF, Bakhshandeh M, Ghorbani M, Mofid B. Assessing the out-of-field dose calculation accuracy by eclipse treatment planning system in sliding window IMRT of prostate cancer patients. Comput Biol Med. 2020.;127:104052. https://doi.org/10.1016/j.compbiomed.2020.104052.
[24] Doležel M, Odrážka K, Vaňásek J, Štuk J, Hlávka A, Vítková M, et al. Long-term clinical results of IGRT in prostate cancer treatment. Klin Onkol. 2020;33(1):49–54https://doi.org/10.14735/amko202049.
[25] Miszczyk M, Majewski W. Hematologic toxicity of conformal radiotherapy and intensity modulated radiotherapy in prostate and bladder cancer patients. Asian Pac J Cancer Prev. 2018;19(10):2803–6https://doi.org/10.22034/apjcp.2018.19.10.2803.
[26] Sini C, Fiorino C, Perna L, Noris Chiorda B, Deantoni CL, Bianchi M, et al. Dose-volume effects for pelvic bone marrow in predicting hematological toxicity in prostate cancer radiotherapy with pelvic node irradiation. Radiother Oncol. 2016;118(1):79–84. https://doi.org/10.1016/j.radonc.2015.11.020.
[27] Quan EM, Li X, Li Y, Wang X, Kudchadker RJ, Johnson JL, et al. A comprehensive comparison of IMRT and VMAT plan quality for prostate cancer treatment. Int J Radiat Oncol Biol Phys. 2012;83(4):1169–78. https://doi.org/10.1016/j.ijrobp.2011.09.015.
[28] Teoh M, Clark CH, Wood K, Whitaker S, Nisbet A. Volumetric modulated arc therapy: a review of current literature and clinical use in practice. Br J Radiol. 2011;84(1007):967–96. https://doi.org/10.1259/bjr/22373346.
[29] Gershkevitsh E, Clark C, Staffurth J, Dearnaley D, Trott K. Dose to bone marrow using IMRT techniques in prostate cancer patients. Strahlenther Onkol. 2005;181(3):172–8. https://doi.org/10.1007/s00066-005-1360-4.
[30] Vlachaki MT, Teslow TN, Amosson C, Uy NW, Ahmad S. IMRT versus conventional 3DCRT on prostate and normal tissue dosimetry using an endorectal balloon for prostate immobilization. Med Dosim. 2005;30(2):69–75. https://doi.org/10.1016/j.meddos.2005.01.002.
[31] International Commission on Radiological Protection. Annals of the ICRP radiological protection in medicine. Elsevier; 2007..
[32] Moquet J, Higueras M, Donovan E, Boyle S, Barnard S, Bricknell C, et al. Dicentric dose estimates for patients undergoing radiotherapy in the RTGene study to assess blood dosimetric models and the new bayesian method for gradient exposure. Radiat Res. 2018;190(6):596 (10.1667%2FRR15116.1).
[33] Taprogge J, Murray I, Gear J, Chittenden SJ, Parker CC, Flux GD. Compartmental model for 223Ra-dichloride in patients with metastatic bone disease from castration-resistant prostate cancer. Int J Radiat Oncol Biol Phys. 2019;105(4):884–92. https://doi.org/10.1016/j.ijrobp.2019.07.022.
[34] Kulka U, Wojcik A. Special issue: networking in biological and EPR/OSL dosimetry: the european RENEB platform for emergency preparedness and research. Int J Radiat Biol. 2017;93(1):1. https://doi.org/10.1080/09553002.2016.1235805.
[35] International Atomic Energy Agency. Cytogenetic dosimetry: applications in preparedness for and response to radiation emergencies. Vienna: IAEA; 2011..
[36] Anderson RM. Cytogenetic biomarkers of radiation exposure. Clin Oncol. 2019;5:311–8. https://doi.org/10.1016/j.clon.2019.02.009.
[37] Turner PG, Jain S, Cole A, Grey A, Mitchell D, Prise KM, et al. Toxicity and efficacy of concurrent androgen deprivation therapy, pelvic radiotherapy, and radium-223 in patients with de novo metastatic hormone-sensitive prostate cancer. Clin Cancer Res. 2021.. https://doi.org/10.1158/1078-0432.CCR-21-0685 Epub ahead of print.
[38] Zimmerman BE, Bergeron DE, Cessna JT, Fitzgerald R, Pibida L. Revision of the NIST standard for (223)Ra: new measurements and review of 2008 data. J Res Natl Inst Stand Technol. 2015;120:37–57 (10.6028%2Fjres.120.004).
[39] Yoshida K, Kaneta T, Takano S, Sugiura M, Kawano T, Hino A, et al. Pharmacokinetics of single dose radium-223 dichloride (BAY 88–8223) in japanese patients with castration-resistant prostate cancer and bone metastases. Ann Nucl Med. 2016;7:453–60 (10.6028%2Fjres.120.004).
[40] Chittenden SJ, Hindorf C, Parker CC, Lewington VJ, Pratt BE, Johnson B, et al. A phase 1, open-label study of the biodistribution, pharmacokinetics, and dosimetry of 223Ra-dichloride in patients with hormone-refractory prostate cancer and skeletal metastases. J Nucl Med. 2015;56(9):1304–9. https://doi.org/10.2967/jnumed.115.157123.
[41] Carrasquillo J, O'Donoghue J, Pandit-Taskar N, Humm J, Rathkopf D, Slovin S, et al. Phase I pharmacokinetic and biodistribution study with escalating doses of 223Ra-dichloride in men with castration-resistant metastatic prostate cancer. Eur J Nucl Med Mol Imaging. 2013;40(9):1384–93. https://doi.org/10.1007/s00259-013-2427-6.
[42] Attix FH. Introduction to radiological physics and radiation dosimetry. 1. Aufl. ed. Wiley-VCH; 2008..
[43] Schumann S, Eberlein U, Muhtadi R, Lassmann M, Scherthan H. DNA damage in leukocytes after internal ex-vivo irradiation of blood with the α-emitter ra-223. Sci Rep. 2018;8(1):2286. https://doi.org/10.1038/s41598-018-20364-7.
[44] Human body weight to volume conversion. Internet. https://www.aqua-calc.com/calculate/weight-to-volume/substance/human-blank-body; 2020. 67. Ann. ICRP.
[45] Sumption ND, Goodhead DT, Anderson RM. No increase in radiation-induced chromosome aberration complexity detected by m-FISH after culture in the presence of 5'-bromodeoxyuridine. Mutat Res. 2006;594(1–2):30–8. https://doi.org/10.1016/j.mrfmmm.2005.07.007.
[46] Perry P, Wolff S. New giemsa method for the differential staining of sister chromatids. Nature. 1974;251(5471):156–8. https://doi.org/10.1038/251156a0.
[47] Themis M, Garimberti E, Hill MA, Anderson RM. Reduced chromosome aberration complexity in normal human bronchial epithelial cells exposed to low-LET γ-rays and high-LET α-particles. Int J Radiat Biol. 2013;89(11):934–43 (10.3109%2F09553002.2013.805889).
[48] Savage JR, Simpson PJ. FISH "painting" patterns resulting from complex exchanges. Mutat Res. 1994;312(1):51–60. https://doi.org/10.1016/0165-1161(94)90008-6.
[49] Anderson RM, Marsden SJ, Paice SJ, Bristow AE, Kadhim MA, Griffin CS, et al. Transmissible and nontransmissible complex chromosome aberrations characterized by three-color and mFISH define a biomarker of exposure to high-LET α particles. Radiat Res. 2003;159(1):40–8. https://doi.org/10.1667/0033-7587(2003)159[0040:TANCCA]2.0.CO;2.
[50] Cornforth MN. Analyzing radiation-induced complex chromosome rearrangements by combinatorial painting. Radiat Res. 2001;155(5):643–59. https://doi.org/10.1667/0033-7587(2001)155[0643:ariccr]2.0.co;2.
[51] Boei JJ, Natarajan AT. Combined use of chromosome painting and telomere detection to analyse radiation-induced chromosomal aberrations in mouse splenocytes. Int J Radiat Biol. 1998;73(2):125–33. https://doi.org/10.1080/095530098142491.
[52] Lloyd DC, Edwards AA, Prosser JS. Chromosome aberrations induced in human lymphocytes by in vitro acute X and gamma radiation. Radiat Prot Dosimetry. 1986;15(2):83–8. https://doi.org/10.1093/oxfordjournals.rpd.a079681.
[53] Ainsbury EA, Lloyd D. Dose estimation software for radiation biodosimetry. Health Phys. 2010;98(2):290–5. https://doi.org/10.1097/01.hp.0000346305.84577.b4.
[54] Purrott RJ, Edwards AA, Lloyd DC, Stather JW. The induction of chromosome aberrations in human lymphocytes by in vitro irradiation with α-particles from Plutonium-239. Int J Radiat Biol. 1980;38(3):277–84. https://doi.org/10.1080/09553008014551641.

[55] Sigurdson AJ, Ha M, Hauptmann M, Bhatti P, Sram RJ, Beskid O, et al. International study of factors affecting human chromosome translocations, 652. ; 2008. p. 112–21. https://doi.org/10.1016/j.mrgentox.2008.01.005 2.
[56] Whitehouse C, Edwards A, Tawn E, Stephan G, Oestreicher U, Moquet J, et al. Translocation yields in peripheral blood lymphocytes from control populations. Int J Radiat Biol. 2005;81(2):139–45. https://doi.org/10.1080/09553000500103082.
[57] Coleman R, Brown J, Rathbone E, Flanagan L, Reid A, Kendall J, et al. CApecitabine plus Radium-223 (Xofigo™) in breast cancer patients with BONe metastases (CARBON): study protocol for a phase IB/IIA randomised controlled trial. Trials. 2020;21(1):89. https://doi.org/10.1186/s13063-019-3643-6.
[58] Geva R, Lopez J, Danson S, Joensuu H, Peer A, Harris SJ, et al. Radium-223 in combination with paclitaxel in cancer patients with bone metastases: safety results from an open-label, multicenter phase ib study. Eur J Nucl Med Mol Imaging. 2018;46(5):1092–101. https://doi.org/10.1007/s00259-018-4234-6.
[59] Huynh-Le M, Shults RC, Connor MJ, Hattangadi-Gluth JA. Adverse events associated with Radium-223 in metastatic prostate cancer: disproportionality analysis of FDA data reflecting worldwide utilization. Clin Genitourin Cancer. 2020;18(3):192–200. https://doi.org/10.1016/j.clgc.2019.11.017 e2.
[60] Soldatos TG, Iakovou I, Sachpekidis C. Retrospective toxicological profiling of Radium-223 dichloride for the treatment of bone metastases in prostate cancer using adverse event data. Medicina (Kaunas). 2019.;55(5). https://doi.org/10.3390/medicina55050149.
[61] Jacene H, Gomella L, Yu EY, Rohren EM. Hematologic toxicity from Radium-223 therapy for bone metastases in castration-resistant prostate cancer: risk factors and practical considerations. Clin Genitourin Cancer. 2018;16(4):e919–26. https://doi.org/10.1016/j.clgc.2018.03.007.
[62] Varkaris A, Gunturu K, Kewalramani T, Tretter C. Acute myeloid leukemia after Radium-223 therapy: case report. Clin Genitourin Cancer. 2017;15(4):e723–6. https://doi.org/10.1016/j.clgc.2016.11.002.
[63] Odo U, Vasudevamurthy AK, Sartor O. Acute promyelocytic leukemia after treatment of metastatic castration-resistant prostate cancer with Radium-223. Clin Genitourin Cancer. 2017;15(3):e501–2. https://doi.org/10.1016/j.clgc.2016.12.028.
[64] Abou DS, Ulmert D, Doucet M, Hobbs RF, Riddle RC, Thorek DLJ. Whole-body and microenvironmental localization of Radium-223 in Naïve and mouse models of prostate cancer metastasis. J Natl Cancer Inst. 2016;108(5):1 (10.1093%2Fjnci%2Fdjv380).
[65] Stephan G, Kampen WU, Noßke D, Roos H. Chromosomal aberrations in peripheral lymphocytes of patients treated with radium-224 for ankylosing spondylitis. Radiat Environ Biophys. 2005;44:23–8.
[66] Schumann S, Eberlein U, Lapa C, Müller J, Serfling S, Lassmann M, et al. α-particle-induced DNA damage tracks in peripheral blood mononuclear cells of [223Ra]RaCl2-treated prostate cancer patients. Eur J Nucl Med Mol Imaging. 2021;48(9):2761–70. https://doi.org/10.1007/s00259-020-05170-6.
[67] ICRP. Age-dependent doses to members of the public from intake of radionuclides - part 2 ingestion dose coefficients. ICRP Publication; 1993. p. 3–4 67. Ann. ICRP.
[68] Hilberath JN, Thomas ME, Smith T, Jara C, Fitzgerald DJ, Wilusz K, et al. Blood volume measurement by hemodilution: association with valve disease and re-evaluation of the Allen formula. Perfusion. 2015;30(4):305–11. https://doi.org/10.1177/0267659114547250.
[69] Moore JE, Bertram CD. Lymphatic system flows. Annu Rev Fluid Mech. 2018;50:459–82. https://doi.org/10.1146/annurev-fluid-122316-045259.
[70] Thwaites D. Accuracy required and achievable in radiotherapy dosimetry: have modern technology and techniques changed our views? J Phys Conf Ser. 2013.;444:012006. https://doi.org/10.1088/1742-6596/444/1/012006.
[71] Bielenberg DR, Zetter BR. The contribution of angiogenesis to the process of metastasis. Cancer J. 2015;21(4):267–73. https://doi.org/10.1097/ppo.0000000000000138.
[72] Chavez-MacGregor M, Aviles-Salas A, Green D, Fuentes-Alburo A, Gómez-Ruiz C, Aguayo A. Angiogenesis in the bone marrow of patients with breast cancer. Clin Cancer Res. 2005;11(15):5396–400. https://doi.org/10.1158/1078-0432.ccr-04-2420.
[73] Mundy GR. Metastasis to bone: causes, consequences and therapeutic opportunities. Nat Rev Cancer. 2002;2(8):584–93. https://doi.org/10.1038/nrc867.
[74] Anderson RM, Stevens DL, Sumption ND, Townsend KMS, Goodhead DT, Hill MA. Effect of linear energy transfer (LET) on the complexity of α-particle-induced chromosome aberrations in human CD34+ cells. Radiat Res. 2007;167(5):541–50. https://doi.org/10.1667/rr0813.1.
[75] Savage JRK, Simpson PJ. Fish "painting" patterns resulting from complex exchanges. Mutat Res. 1994;312(1):51–60. https://doi.org/10.1016/0165-1161(94)90008-6.
[76] Savage JRK, Simpson P. On the scoring of FISH-"painted" chromosome-type exchange aberrations. Mutat Res Fundam Mol Mech Mutagen. 1994;307(1):345–53. https://doi.org/10.1016/0027-5107(94)90308-5.
[77] Barquinero JF, Stephan G, Schmid E. Effect of americium-241 α-particles on the dose–response of chromosome aberrations in human lymphocytes analysed by fluorescence in situ hybridization. Int J Radiat Biol. 2004;80(2):155–64. https://doi.org/10.1080/09553002310001655430.
[78] Moquet JE, Fernández JL, Edwards AA, Lloyd DC. Lymphocyte chromosomal aberrations and their complexity induced in vitro by plutonium-239 alpha-particles and detected by FISH. Cell Mol Biol (Noisy-le-Grand). 2001;47(3):549–56.
[79] Anderson RM, Marsden SJ, Wright EG, Kadhim MA, Goodhead DT, Griffin CS. Complex chromosome aberrations in peripheral blood lymphocytes as a potential biomarker of exposure to high-LET alpha-particles. Int J Radiat Biol. 2000;76(1):31–42. https://doi.org/10.1080/095530000138989.
[80] Testard I, Dutrillaux B, Sabatier L. Chromosomal aberrations induced in human lymphocytes by high-LET irradiation. Int J Radiat Biol. 1997;72(4):423–33. https://doi.org/10.1080/095530097143194.
[81] Griffin CS, Marsden SJ, Stevens DL, Simpson P, Savage JRK. Frequencies of complex chromosome exchange aberrations induced by 238Pu α-particles and detected by fluorescence in situ hybridization using single chromosome-specific probes. Int J Radiat Biol. 1995;67(4):431–9. https://doi.org/10.1080/09553009514550491.
[82] Loucas BD, Durante M, Bailey SM, Cornforth MN. Chromosome damage in human cells by γ rays, α particles and heavy ions: track interactions in basic dose-response relationships. Radiat Res. 2013;179(1):9–20 (10.1667%2FRR3089.1).
[83] Loucas BD, Cornforth MN. Complex chromosome exchanges induced by gamma rays in human lymphocytes: an mFISH study. Radiat Res. 2001;155(5):660–71. https://doi.org/10.1667/0033-7587(2001)155[0660:cceibg]2.0.co;2.
[84] Pignalosa D, Lee R, Hartel C, Sommer S, Nikoghosyan A, Debus J, et al. Chromosome inversions in lymphocytes of prostate cancer patients treated with X-rays and carbon ions. Radiother Oncol. 2013;109(2):256–61. https://doi.org/10.1016/j.radonc.2013.09.021.
[85] Hartel C, Nikoghosyan A, Durante M, Sommer S, Nasonova E, Fournier C, et al. Chromosomal aberrations in peripheral blood lymphocytes of prostate cancer patients treated with IMRT and carbon ions. Radiother Oncol. 2009;95(1):73–8. https://doi.org/10.1016/j.radonc.2009.08.031.
[86] Sanguineti G, Giannarelli D, Petrongari MG, Arcangeli S, Sangiovanni A, Saracino B, et al. Leukotoxicity after moderately hypofractionated radiotherapy versus conventionally fractionated dose escalated radiotherapy for localized prostate cancer: a secondary analysis from a randomized study. Radiat Oncol. 2019.;14. https://doi.org/10.1186/s13014-019-1223-2.
[87] Landoni V, Fiorino C, Cozzarini C, Sanguineti G, Valdagni R, Rancati T. Predicting toxicity in radiotherapy for prostate cancer. Phys Med. 2016;32(3):521–32. https://doi.org/10.1016/j.ejmp.2016.03.003.
[88] Pinkawa M, Djukic V, Klotz J, Petz D, Piroth MD, Holy R, et al. Hematologic changes during prostate cancer radiation therapy are dependent on the treatment volume. Future Oncol. 2014;10(5):835–43. https://doi.org/10.2217/fon.13.237.
[89] Canter BS, Leung CN, Fritton JC, Bäck T, Rajon D, Azzam EI, et al. Radium-223-induced bystander effects cause DNA damage and apoptosis in disseminated tumor cells in bone marrow. Mol Cancer Res. 2021.. https://doi.org/10.1158/1541-7786.MCR-21-0005 Epub ahead of print.